



Entangled atomic ensemble and an yttrium-iron-garnet sphere in coupled microwave cavitiesDilawaiz,¹ Shahid Qamar,^{1,2} and Muhammad Irfan ^{1,2,*}¹*Department of Physics and Applied Mathematics, Pakistan Institute of Engineering and Applied Sciences, Nilore 45650, Islamabad, Pakistan*²*Center for Mathematical Sciences, PIEAS, Nilore, Islamabad 45650, Pakistan* (Received 3 March 2023; revised 12 October 2023; accepted 25 March 2024; published 10 April 2024)

We present a scheme to generate distant bipartite and tripartite entanglement between an atomic ensemble and an yttrium iron garnet (YIG) sphere in coupled microwave cavities. We consider an atomic ensemble in a single-mode microwave cavity which is coupled with a second single-mode cavity having a YIG sphere. Our system, therefore, has five excitation modes, namely, cavity-1 photons, an atomic ensemble, cavity-2 photons, a magnon and a phonon mode in the YIG sphere. We show that significant bipartite entanglement exists between indirectly coupled subsystems in the cavities which is robust against temperature. Moreover, we present suitable parameters for a significant tripartite entanglement of the ensemble, magnon, and phonon modes. We also demonstrate the existence of tripartite entanglement between the magnon and phonon modes of the YIG sphere with indirectly coupled cavity photons. Interestingly, this distant tripartite entanglement is of the same order as that previously found for a single-cavity system. We show that cavity-cavity coupling strength affects both the degree and transfer of quantum entanglement between various subsystems. Therefore, an appropriate cavity-cavity coupling optimizes the distant entanglement by increasing the entanglement strength and its robustness against temperature.

DOI: [10.1103/PhysRevA.109.043708](https://doi.org/10.1103/PhysRevA.109.043708)**I. INTRODUCTION**

Quantum entanglement is recognized as the most fascinating aspect of quantum formalism [1]. It has applications in quantum information processing, quantum networking, quantum dense coding, quantum-enhanced metrology, and so on [2–5]. Therefore, its realization through physical resources used in information processing and communication protocols necessitates a scale above the subatomic level for the ease of experimental implementation [6]. That is why there is growing attention to the exploration of quantum-mechanical effects at the macroscopic level. The advancement in micro- and nanofabrication in recent years provided novel platforms to study macroscopic entanglement. Cavity optomechanics is one such system that received a lot of attention during the past decade [7,8]. Among other applications [9,10], cavity optomechanics enables quantum state transfer between different modes of electromagnetic fields [11,12], which has a central role in quantum information-processing networks. Moreover, a possible platform for quantum information processing is offered by atomic ensembles. They can serve as valuable memory nodes for quantum communication networks due to their longer coherence duration and collective amplification effect [13]. Another promising physical platform is yttrium iron garnet (YIG), a ferrimagnetic material, due to its high spin density and low decay rates of collective spin excitations (i.e., the Kittel mode [14]), resulting in strong coupling between the Kittel mode and cavity photons [15–18].

Since the initial experiments, many hybrid quantum systems based on quantum magnonics have been studied for their possible applications in quantum technologies [19–22]. Magnon-cavity QED is a relatively newer field and a potential candidate for studying new features of strong-coupling QED. The observation of bistability and the single superconducting qubit coupling to the Kittel mode are interesting developments in this field [23,24]. Li *et al.* illustrated how to create tripartite entanglement in a system of microwave cavity photons entangled to the magnon and phonon modes of a YIG sphere in a magnomechanical cavity [25]. This study was followed by an investigation of magnon-magnon entanglement between two YIG spheres in cavity magnomechanics [26]. Later, Wu *et al.* investigated magnon-magnon entanglement between two YIG spheres in cavity optomagnonics [27]. Likewise, Ning and Yin theoretically demonstrated the entanglement of a magnon and superconducting qubit utilizing a two-mode squeezed-vacuum microwave field in coupled cavities [28]. Wang *et al.* explored nonreciprocal transmission and entanglement in a two-cavity magnomechanical system [29]. That work was succeeded by the study of long-range generation of magnon-magnon entangled states via qubits [30].

Potential schemes for distant entanglement between separate systems are increasingly being considered to test the fundamental limits of quantum theory and possible applications in quantum networks [31]. In an interesting study, Joshi *et al.* theoretically examined whether two spatially distant cavities connected by an optical fiber may produce quantum entanglement between mechanical and optical modes [32]. Likewise, many researchers theoretically explored other schemes for transferring entanglement at a distance which

*Corresponding author: m.irfanphy@gmail.com

includes an array of three optomechanical cavities for the study of the entanglement between different mechanical and optical modes [33] and a doubly resonant cavity with a gain medium of cascading three-level atoms placed in it to investigate entanglement transfer from two-mode fields to the two movable mirrors [34]. In a double-cavity optomechanical system, Liao *et al.* quantified the entanglement of macroscopic mechanical resonators by the concurrence [35]. That work was followed by a study on entanglement transfer from the intercavity photon-photon entanglement to an intracavity photon-phonon via two macroscopic mechanical resonators [36]. Recently, Bai *et al.* proposed a scheme for a two-cavity coupled optomechanical system with an atomic ensemble and a movable mirror in distinct cavities, through which they showed ensemble-mirror entanglement and entanglement transfer between different subsystems [37].

In the past, several cavity optomechanical systems were studied for entanglement with an atomic medium [37–40]. Recently, it was shown that an atomic ensemble can be entangled with magnon modes within a single cavity [41,42]. However, to the best of our knowledge, distant entanglement of an atomic ensemble and YIG sphere in microwave cavities has not been reported yet. In this paper, we present a method for entangling an atomic ensemble to mechanical and Kittel modes in a YIG sphere placed within coupled microwave cavities. In our study, we consider an atomic ensemble containing $N \sim 10^7$ [43,44] atoms and a YIG sphere with a typical diameter of 250 μm [45], a promising platform for studying distant macroscopic entanglement. We show that significant bipartite and tripartite entanglement exists between the magnon and phonon modes of the YIG sphere placed in cavity 2 and the atomic ensemble and cavity-1 photons. It is interesting to find that a YIG sphere can be entangled to an indirectly coupled cavity field. We illustrate that this distant entanglement can be controlled by varying the cavity-cavity coupling strength. Since atomic ensembles can serve as efficient memory nodes for quantum communication networks, we therefore believe that the considered hybrid system has useful applications in quantum technologies.

II. SYSTEM MODEL AND HAMILTONIAN

We consider a hybrid coupled-cavity magnomechanical system which consists of two single-mode cavities with resonance frequency ω_k ($k = 1, 2$) encasing an atomic ensemble and a YIG sphere as shown in Fig. 1. This coupled system has five excitation modes, namely, microwave electromagnetic modes in cavities 1 and 2, magnon and phonon modes in the YIG sphere, and atomic excitation in cavity 1.

In cavity 2, a YIG sphere is placed close to the maximum magnetic field of the cavity mode and is simultaneously acted upon by a bias magnetic field, thus establishing the photon-magnon coupling. The external bias magnetic field excites the magnon modes. The magnetic field of the cavity mode interacts with the Kittel mode via the magnetic dipole interaction, in which spins evenly precess in the ferrimagnetic sphere. The bias field \mathbf{B} and the gyromagnetic ratio Γ control the magnon frequency, i.e., $\omega_n = \Gamma\mathbf{B}$. Varying magnetization in the YIG sphere results in magnetostriction, leading to the interplay of energy between the magnon and phonon modes in it.

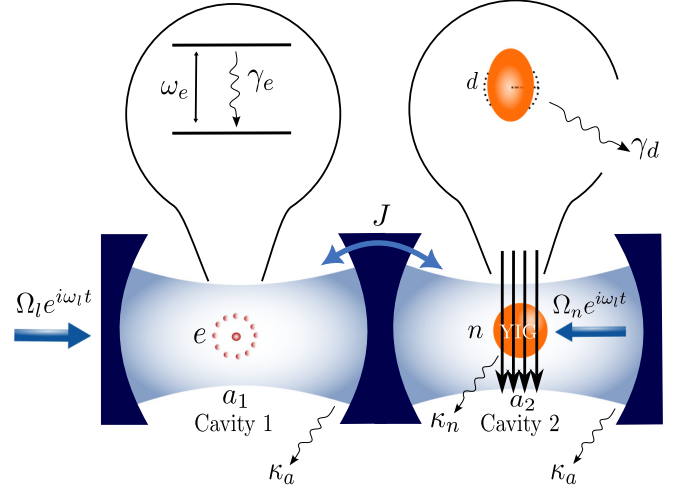


FIG. 1. Schematic representation of two single-mode cavities coupled to each other with coupling strength J incorporating an atomic ensemble of N two-level atoms characterized by intrinsic frequency ω_e placed in cavity 1 and a YIG sphere placed in cavity 2. An external laser field drives the cavity at frequency ω_l with strength Ω_l . Correspondingly, a microwave magnetic field at frequency ω_l with strength Ω_n drives the magnon modes of the YIG sphere, enhancing the magnomechanical coupling. The YIG sphere is concurrently influenced by the cavity's magnetic field, the bias magnetic field, and the drive magnetic field, all orthogonal to each other at the site of the YIG sphere. The decay rates of the cavity modes a_1 and a_2 , atomic ensemble e , magnon mode n , and phonon mode d associated with the YIG sphere are given by κ_a , γ_e , κ_n , and γ_d , respectively.

In cavity 1, an ensemble of N two-level atoms with transition frequency ω_e interacts with the cavity field. The atoms constituting the ensemble are individually characterized by the spin-1/2 Pauli matrices σ_+ , σ_- , and σ_z . Collective spin operators of the atomic polarization for the atomic ensemble are described as $S_{+,-,z} = \sum_{i=1}^N \sigma_{+,-,z}^{(i)}$, and they follow the commutation relations $[S_+, S_-] = S_z$ and $[S_z, S_{\pm}] = \pm 2S_{\pm}$ [37]. The operators S_{\pm} and S_z may be represented in terms of the bosonic annihilation and creation operators e and e^\dagger by using the Holstein-Primakoff transformation [46–48]: $S_+ = e^\dagger \sqrt{N - e^\dagger e} \simeq \sqrt{N} e^\dagger$, $S_- = \sqrt{N - e^\dagger e} e \simeq \sqrt{N} e$, $S_z = e^\dagger e - N/2$, where e and e^\dagger follow the commutation relation $[e, e^\dagger] = 1$. This transformation is valid only when the population of atoms in the ground state is large compared to the atoms in the excited state, so that $S_z \simeq \langle S_z \rangle \simeq -N$ [43].

To simplify our analysis, we consider the frequencies of both the drive laser field and the drive magnetic field to be ω_l . The Hamiltonian describing the system under the rotating-wave approximation in a frame rotating with the frequency of the drive fields ω_l is given by

$$\begin{aligned}
 H/\hbar = & \sum_{k=1}^2 \Delta_k a_k^\dagger a_k + \Delta_e e^\dagger e + \Delta_n n^\dagger n + \frac{\omega_d}{2} (x^2 + y^2) \\
 & + g_{nd} n^\dagger n x + J(a_1^\dagger a_2 + a_1 a_2^\dagger) + G_{ae} (e a_1^\dagger + e^\dagger a_1) \\
 & + g_{na} (a_2 n^\dagger + a_2^\dagger n) + i\Omega_l (a_1^\dagger - a_1) + i\Omega_n (n^\dagger - n).
 \end{aligned} \tag{1}$$

In Eq. (1), the energy associated with the cavity (1 and 2), atomic excitation, and magnon modes is represented in the first three terms, where a_k (a_k^\dagger), e (e^\dagger), and n (n^\dagger) are the annihilation (creation) operators of the cavity, collective atomic excitation, and magnon mode, respectively. Here, Δ_k ($k = 1, 2$), Δ_e , and Δ_n are the detunings of the cavity mode's frequency ω_k ($k = 1, 2$), the intrinsic frequency of two-level atoms in the atomic ensemble ω_e , and the magnon mode's frequency ω_n with respect to the drive field's frequency ω_l , i.e., $\Delta_k = \omega_k - \omega_l$ ($k = 1, 2$), $\Delta_e = \omega_e - \omega_l$, and $\Delta_n = \omega_n - \omega_l$. The rotating-wave approximation holds when ω_k ($k = 1, 2$), ω_n , $\omega_e \gg g_{na}, \kappa_a, \kappa_n, \gamma_e$ (which is satisfied in cavity magnomechanics by experimentally feasible parameters) [49]. The fourth term in Eq. (1) is the energy of the mechanical mode (phonon mode) of frequency ω_d with dimensionless position x and momentum y operators satisfying $[x, y] = i$. The next four terms describe the interaction of all coupled subsystems in the cavity system encompassing coupling of the magnon and phonon, cavities 1 and 2, collective atomic excitation and cavity 1, and cavity 2 and magnon modes with strengths g_{nd} , J , G_{ae} , and g_{na} , respectively. The magnomechanical coupling strength g_{nd} , resulting from magnetostrictive interaction, is typically weak; however, it can be enhanced by the drive microwave field having frequency ω_l applied at the site of the YIG. The coupling rate of the collective atomic excitation with cavity mode $G_{ae} = g\sqrt{N}$, where g is the atom-cavity coupling strength, defined as $g = v\sqrt{\omega_l/2\hbar\epsilon_0 V}$, with v being the dipole moment of atomic transition, V being the volume of the cavity, and ϵ_0 being the permittivity of free space. Regarding the eighth term (magnon-photon coupling), when the coherent energy exchange rate between light and matter is faster than their decay rates, the coupling strength between the magnon and photon reaches the strong-coupling regime, i.e., $g_{na} > \kappa_a, \kappa_n$ [14,15,17,18,49]. The second-to-last term describes a microwave field driving cavity 1 with Rabi frequency $\Omega_l = \sqrt{2P\kappa_a/\hbar\omega_l}$, which depends on the input power P of the drive field and the decay rate κ_a of the cavity. Similarly, we also consider a magnon-mode drive field [last term in Eq. (1)] with Rabi frequency $\Omega_n = \frac{\sqrt{5}}{4}\Gamma\sqrt{N_s}B_0$, with Γ being the gyromagnetic ratio, N_s being the total number of spins, and B_0 being the applied field's amplitude. In the case of a YIG sphere,

$\Gamma/2\pi = 28$ GHz/T, and $N_s = \rho V_s$, with volume V_s and spin density $\rho = 4.22 \times 10^{27} \text{ m}^{-3}$ of the sphere [25]. We assume low-lying excitations while deriving Ω_n , i.e., $\langle n^\dagger n \rangle \ll 2N_s\zeta$, where $\zeta = \frac{5}{2}$ is the spin number of the ground-state Fe^{3+} ion in YIG [25]. At a temperature T , the equilibrium mean thermal photon [a_k ($k = 1, 2$)], magnon (n), and phonon (d) numbers are given by $Z_h(\omega_h) = [\exp(\hbar\omega_h/k_B T) - 1]^{-1}$ ($h = a_k, n, d$), where k_B is the Boltzmann constant.

Since, we are interested in studying steady-state quantum entanglement in the linear regime, we use standard input-output theory resulting in quantum Langevin equations in which the effect of the input noise operator is added for each excitation mode:

$$\begin{aligned}\dot{a}_1 &= -(\kappa_a + i\Delta_1)a_1 - iG_{ae}e - iJa_2 + \sqrt{2\kappa_a}a_1^{\text{in}} + \Omega_l, \\ \dot{a}_2 &= -(\kappa_a + i\Delta_2)a_2 - iJa_1 - ig_{na}n + \sqrt{2\kappa_a}a_2^{\text{in}}, \\ \dot{e} &= -(\gamma_e + i\Delta_e)e - iG_{ae}a_1 + \sqrt{2\gamma_e}e^{\text{in}}, \\ \dot{n} &= -(i\Delta_n + \kappa_n)n - ig_{na}a_2 - ig_{nd}nx + \Omega_n + \sqrt{2\kappa_n}n^{\text{in}}, \\ \dot{x} &= \omega_d y, \quad \dot{y} = -\omega_d x - \gamma_d y - g_{nd}n^\dagger n + \xi,\end{aligned}\quad (2)$$

with zero-mean input noise operators a_k^{in} , e^{in} , n^{in} , and ξ for the k th cavity, atomic-excitation, magnon, and phonon modes, respectively. The parameters γ_e and γ_d are the atomic decay rate and the mechanical damping rate, respectively. The input noise operators under Markovian approximation, which is valid for a large mechanical quality factor, $Q = \omega_d/\gamma_d \gg 1$, are characterized by the following nonvanishing correlation functions that are δ correlated in the time domain [50]: $\langle a_1^{\text{in}}(\tau)a_1^{\text{in}\dagger}(\tau') \rangle = [Z_{a_1}(\omega_{a_1}) + 1]\delta(\tau - \tau')$, $\langle a_1^{\text{in}\dagger}(\tau)a_1^{\text{in}}(\tau') \rangle = Z_{a_1}(\omega_{a_1})\delta(\tau - \tau')$, $\langle a_2^{\text{in}}(\tau)a_2^{\text{in}\dagger}(\tau') \rangle = [Z_{a_2}(\omega_{a_2}) + 1]\delta(\tau - \tau')$, $\langle a_2^{\text{in}\dagger}(\tau)a_2^{\text{in}}(\tau') \rangle = Z_{a_2}(\omega_{a_2})\delta(\tau - \tau')$, $\langle e^{\text{in}}(\tau)e^{\text{in}\dagger}(\tau') \rangle = \delta(\tau - \tau')$, $\langle n^{\text{in}}(\tau)n^{\text{in}\dagger}(\tau') \rangle = [Z_n(\omega_n) + 1]\delta(\tau - \tau')$, $\langle n^{\text{in}\dagger}(\tau)n^{\text{in}}(\tau') \rangle = Z_n(\omega_n)\delta(\tau - \tau')$, and $\langle \xi(\tau)\xi(\tau') + \xi(\tau')\xi(\tau) \rangle / 2 \simeq \gamma_d [2Z_d(\omega_d) + 1]\delta(\tau - \tau')$, where τ and τ' denote two distinct times. It is important to note that the δ -correlated mechanical noise approximation is valid only for a large mechanical quality factor. For the case of a low-quality factor, we have to solve for the exact correlation function of the noise operators.

From the quantum Langevin equations (2), we obtain the expressions for the steady-state values of the cavity, ensemble, magnon, and phonon mode operators:

$$\begin{aligned}\langle a_1 \rangle &= \frac{\Omega_l(\kappa_a + i\Delta_2)(\kappa_n + i\tilde{\Delta}_n)(\gamma_e + i\Delta_e) + g_{na}^2\Omega_l(\gamma_e + i\Delta_e) - g_{na}\Omega_n J(\gamma_e + i\Delta_e)}{S}, \\ \langle a_2 \rangle &= \frac{-iJ(\kappa_n + i\tilde{\Delta}_n)\langle a_1 \rangle - ig_{na}\Omega_n}{(\kappa_a + i\Delta_2)(\kappa_n + i\tilde{\Delta}_n) + g_{na}^2}, \quad \langle e \rangle = \frac{-iG_{ae}\langle a_1 \rangle}{(\gamma_e + i\Delta_e)}, \quad \langle n \rangle = \frac{\Omega_n - ig_{na}\langle a_2 \rangle}{i\tilde{\Delta}_n + \kappa_n}, \\ \langle x \rangle &= -\left(\frac{g_{nd}}{\omega_d}\right)|\langle n \rangle|^2, \quad \langle y \rangle = 0,\end{aligned}\quad (3)$$

where

$$S = (\kappa_a + i\Delta_1)(\gamma_e + i\Delta_e)[(\kappa_a + i\Delta_2)(\kappa_n + i\tilde{\Delta}_n) + g_{na}^2] - G_{ae}^2[(\kappa_a + i\Delta_2)(\kappa_n + i\tilde{\Delta}_n) + g_{na}^2] + J^2(\gamma_e + i\Delta_e)(\kappa_n + i\tilde{\Delta}_n)$$

and the effective magnon detuning $\tilde{\Delta}_n = \Delta_n + g_{nd}\langle x \rangle$. The effective magnomechanical coupling rate is $G_{nd} = i\sqrt{2}g_{nd}\langle n \rangle$.

To analyze the steady-state entanglement of the system, we linearize the dynamics of the coupled cavity system. We

assume that the cavity is intensely driven with a very high input power, resulting in significant steady-state amplitudes for the intracavity fields and magnon modes, respectively, i.e., $|\langle a_k \rangle| \gg 1$ ($k = 1, 2$) [51] and $|\langle n \rangle| \gg 1$ [25]. For a proper choice of the drive field's reference phase, $\langle a_k \rangle$ may be treated as real [51]. Moreover, the bosonic description of atomic polarization may be used only when the single-atom excitation probability is noticeably below 1. The conditions for large steady-state amplitudes of intracavity fields and a low excitation limit of atoms in the ensemble are simultaneously satisfied only when $g^2/(\Delta_e^2 + \gamma_e^2) \ll |\langle a_1 \rangle|^{-2} \ll 1$. This necessitates a weak atom-cavity coupling [43]. Hence, in the strong-driving limit, we can neglect the second-order fluctuation terms, such that the operator P ($P = a_k, e, n, x, y$) can be written as $P = \langle P \rangle + \delta P$, where $\langle P \rangle$ represents the steady-state part and δP represents the zero-mean fluctuation associated with P . In the opposite limit where the quantum effects of a single or few excitations are important [52,53] or in studying a fully nonlinear Hamiltonian [54], the standard quantum master equation may be used to study the

dynamics of the system. Similarly, coupling with a nonequilibrium environment also requires exact quantum Langevin equations [55]. Next, we define quadrature fluctuations $[\delta U_1(t), \delta W_1(t), \delta U_2(t), \delta W_2(t), \delta u_1(t), \delta w_1(t), \delta x(t), \delta y(t), \delta u_2(t), \delta w_2(t)]$, with $\delta U_1 = (\delta a_1 + \delta a_1^\dagger)/\sqrt{2}$, $\delta W_1 = i(\delta a_1^\dagger - \delta a_1)/\sqrt{2}$, $\delta U_2 = (\delta a_2 + \delta a_2^\dagger)/\sqrt{2}$, $\delta W_2 = i(\delta a_2^\dagger - \delta a_2)/\sqrt{2}$, $\delta u_1 = (\delta n + \delta n^\dagger)/\sqrt{2}$, $\delta w_1 = i(\delta n^\dagger - \delta n)/\sqrt{2}$, $\delta u_2 = (\delta e + \delta e^\dagger)/\sqrt{2}$, and $\delta w_2 = i(\delta e^\dagger - \delta e)/\sqrt{2}$, to work out a set of linearized quantum Langevin equations

$$\dot{r}(t) = Ar(t) + o(t), \quad (4)$$

with $r(t)$ being the fluctuation operator in the form of quadrature fluctuations, where $r(t)^T = [\delta U_1(t), \delta W_1(t), \delta U_2(t), \delta W_2(t), \delta u_1(t), \delta w_1(t), \delta x(t), \delta y(t), \delta u_2(t), \delta w_2(t)]$; $o(t)$ denotes the noise operators, represented as $o(t)^T = [\sqrt{2\kappa_a} U_1^{\text{in}}(t), \sqrt{2\kappa_a} W_1^{\text{in}}(t), \sqrt{2\kappa_a} U_2^{\text{in}}(t), \sqrt{2\kappa_a} W_2^{\text{in}}(t), \sqrt{2\kappa_n} u_1^{\text{in}}(t), \sqrt{2\kappa_n} w_1^{\text{in}}(t), 0, \xi(t), \sqrt{2\gamma_e} u_2^{\text{in}}(t), \sqrt{2\gamma_e} w_2^{\text{in}}(t)]$; and A is the drift matrix:

$$A = \begin{pmatrix} -\kappa_a & \Delta_1 & 0 & J & 0 & 0 & 0 & 0 & 0 & 0 & G_{ae} \\ -\Delta_1 & -\kappa_a & -J & 0 & 0 & 0 & 0 & 0 & -G_{ae} & 0 & 0 \\ 0 & J & -\kappa_a & \Delta_2 & 0 & g_{na} & 0 & 0 & 0 & 0 & 0 \\ -J & 0 & -\Delta_2 & -\kappa_a & -g_{na} & 0 & 0 & 0 & 0 & 0 & 0 \\ 0 & 0 & 0 & g_{na} & -\kappa_n & \tilde{\Delta}_n & -G_{nd} & 0 & 0 & 0 & 0 \\ 0 & 0 & -g_{na} & 0 & -\tilde{\Delta}_n & -\kappa_n & 0 & 0 & 0 & 0 & 0 \\ 0 & 0 & 0 & 0 & 0 & 0 & 0 & \omega_d & 0 & 0 & 0 \\ 0 & 0 & 0 & 0 & 0 & G_{nd} & -\omega_d & -\gamma_d & 0 & 0 & 0 \\ 0 & G_{ae} & 0 & 0 & 0 & 0 & 0 & 0 & -\gamma_e & \Delta_e & 0 \\ -G_{ae} & 0 & 0 & 0 & 0 & 0 & 0 & 0 & -\Delta_e & -\gamma_e & 0 \end{pmatrix}. \quad (5)$$

The linearized quantum Langevin equations [see Eq. (4)] correspond to an effective linearized Hamiltonian, which ensures the Gaussian state of the system when it is stable. Thus, the linearized dynamics of the system along with the Gaussian nature of the noises leads to the continuous-variable five-mode Gaussian state of the steady states corresponding to its quantum fluctuations. The Routh-Hurwitz criterion is used to work out the stability conditions for our linearized system [56]. The system becomes stable and attains its steady state only when the real parts of all the eigenvalues of the drift matrix A are negative. The steady-state covariance matrix (CM), which describes the variance within each subsystem and the covariance across several subsystems, is generated from the following Lyapunov equation when the stability requirements are met [57]:

$$AV + \mathcal{V}A^T = -D, \quad (6)$$

where $D = \text{diag}[\kappa_a(2Z_a + 1), \kappa_a(2Z_a + 1), \kappa_a(2Z_a + 1), \kappa_a(2Z_a + 1), \kappa_n(2Z_n + 1), \kappa_n(2Z_n + 1), 0, \gamma_d(2Z_d + 1), \gamma_e, \gamma_e]^T$ is the diffusion matrix for the corresponding decays originating from the noise correlations.

To quantify bipartite entanglement among different subsystems of the coupled two-cavity system, we use logarithmic negativity E_N [58,59]. We have a five-mode Gaussian state characterized by a covariance matrix \mathcal{V} which can be

expressed in the form of a block matrix:

$$\mathcal{V} = \begin{pmatrix} \mathcal{V}_{a_1} & \mathcal{V}_{a_1 a_2} & \mathcal{V}_{a_1 n} & \mathcal{V}_{a_1 d} & \mathcal{V}_{a_1 e} \\ \mathcal{V}_{a_1 a_2}^T & \mathcal{V}_{a_2} & \mathcal{V}_{a_2 n} & \mathcal{V}_{a_2 d} & \mathcal{V}_{a_2 e} \\ \mathcal{V}_{a_1 n}^T & \mathcal{V}_{a_2 n}^T & \mathcal{V}_n & \mathcal{V}_{nd} & \mathcal{V}_{ne} \\ \mathcal{V}_{a_1 d}^T & \mathcal{V}_{a_2 d}^T & \mathcal{V}_{nd}^T & \mathcal{V}_d & \mathcal{V}_{de} \\ \mathcal{V}_{a_1 e}^T & \mathcal{V}_{a_2 e}^T & \mathcal{V}_{ne}^T & \mathcal{V}_{de}^T & \mathcal{V}_e \end{pmatrix}, \quad (7)$$

where each block is a 2×2 matrix. Here, diagonal blocks represent the variance within each subsystem (cavity-1 photon, cavity-2 photon, magnon, phonon, and ensemble). The correlations between any two distinct degrees of freedom of the entire magnomechanical system are represented by the off-diagonal blocks, which are covariances across distinct subsystems [37]. Following Simon's criterion [60] to judge the nonseparability of the transposed modes in the transposed submatrix derived from the covariance matrix \mathcal{V} , we compute the logarithmic negativity numerically. The covariance matrix \mathcal{V} (10×10) is reduced to a submatrix \mathcal{V}_l (4×4) in order to evaluate the covariance between the subsystems. For instance, the submatrix representing the covariance of cavity-1 and cavity-2 subsystems is determined by the first four rows and columns of \mathcal{V} . We can represent \mathcal{V}_l of cavity-1 and cavity-2

subsystems in the following way [37]:

$$\mathcal{V}_l = \begin{pmatrix} \mathcal{V}_{a_1} & \mathcal{V}_{a_1 a_2} \\ \mathcal{V}_{a_1 a_2}^T & \mathcal{V}_{a_2} \end{pmatrix}, \quad (8)$$

where a_1 indexes the cavity-1 subsystem and a_2 indexes the cavity-2 subsystem. Similarly, the covariance of other subsystems can be determined by considering their corresponding rows and columns in \mathcal{V} . Then, the transposed covariance submatrix $\tilde{\mathcal{V}}_l$ is obtained by partial transposition of \mathcal{V}_l employing $\tilde{\mathcal{V}}_l = \mathcal{T}_{1|2} \mathcal{V}_l \mathcal{T}_{1|2}$, where $\mathcal{T}_{1|2} = \text{diag}(1, -1, 1, 1)$ realizes partial transposition at the level of covariance matrices [60]. Then, we compute the minimum symplectic eigenvalue \tilde{f}_- of the transposed CM $\tilde{\mathcal{V}}_l$ using $\tilde{f}_- = \min \text{eig} |i\Theta_2 \tilde{\mathcal{V}}_l|$, with $\Theta_2 = \bigoplus_{j=1}^2 i\sigma_y$ and σ_y being the y -Pauli matrix [25]. If the smallest eigenvalue is less than $1/2$, the inseparability of the transposed modes is ensured; i.e., the modes are entangled. E_N is evaluated as [59]

$$E_N \equiv \max[0, -\ln 2\tilde{f}_-]. \quad (9)$$

Similarly, the residual contangle \mathcal{R}_τ^{\min} [61], which is a continuous-variable analog of the tangle for discrete-variable tripartite entanglement [62], is used for the quantification of tripartite entanglement, which is defined as [61]

$$\mathcal{R}_\tau^{\min} \equiv \min [\mathcal{R}_\tau^{o|nd}, \mathcal{R}_\tau^{n|od}, \mathcal{R}_\tau^{d|on}], \quad (10)$$

where n stands for the magnon mode and d stands for the phonon mode, $o = a_1$ for cavity-magnon-phonon tripartite entanglement, and $o = e$ for magnon-phonon-ensemble tripartite entanglement. In Eq. (10) $\mathcal{R}_\tau^{k|lm}$ is evaluated using $\mathcal{R}_\tau^{k|lm} \equiv C_{k|lm} - C_{k|l} - C_{k|m}$ ($k, l, m = o, n, d$), $C_{k|lm}$ is the square one-mode-vs-two-mode logarithmic negativity $E_{k|lm}$, and $C_{k|l}$ is the contangle of subsystems of k and l [25], defined as the square logarithmic negativity $E_{k|l}$ [59]. To compute $E_{k|lm}$ following the definition of logarithmic negativity given in Eq. (9), $\Theta_2 = \bigoplus_{j=1}^2 i\sigma_y$ is replaced by $\Theta_3 = \bigoplus_{j=1}^3 i\sigma_y$, and the transposed covariance matrix $\tilde{\mathcal{V}}$ is obtained by carrying out the partial transposition of the covariance matrix \mathcal{V} , i.e., $\tilde{\mathcal{V}} = \mathcal{T}_{k|lm} \mathcal{V} \mathcal{T}_{k|lm}$, where the partial transposition matrices [25] are $\mathcal{T}_{1|23} = \text{diag}(1, -1, 1, 1, 1, 1)$, $\mathcal{T}_{2|13} = \text{diag}(1, 1, 1, -1, 1, 1)$, and $\mathcal{T}_{3|12} = \text{diag}(1, 1, 1, 1, 1, -1)$.

III. RESULTS AND DISCUSSION

In this section, we present the results of our numerical simulations. We have adopted the following experimentally feasible parameters for the system involving microwave cavities and a YIG sphere in our simulations [25]: $\omega_k/2\pi = \omega_n/2\pi = 10$ GHz ($k = 1, 2$), $\omega_d/2\pi = 10$ MHz, $\gamma_d/2\pi = 10^2$ Hz, $\kappa_a/2\pi = \kappa_n/2\pi = 1$ MHz, $g_{na}/2\pi = 3.2$ MHz, $G_{nd}/2\pi = 4.8$ MHz, and temperature $T = 10$ mK. Correspondingly, the atom-cavity coupling and atomic decay rate are considered to be of the order of megahertz, i.e., $G_{ae}/2\pi = 6$ MHz and $\gamma_e/2\pi = 1$ MHz. Further, the hopping rate J between the cavities is also of the order of megahertz. It can be seen that for the above-chosen parameters, our system is well within the low-excitation regime of an atomic ensemble, satisfying the condition $g^2/(\Delta_e^2 + \gamma_e^2) \ll 1$.

First, we discuss the results of bipartite entanglement. We have five different modes in the coupled-cavity

TABLE I. Notation adopted for the representation of bipartite entanglement.

Bipartite subsystem	Symbol for entanglement
Cavity-1–magnon	$E_N^{a_1 n}$
Cavity-1–phonon	$E_N^{a_1 d}$
Cavity-2–magnon	$E_N^{a_2 n}$
Cavity-2–phonon	$E_N^{a_2 d}$
Magnon-ensemble	E_N^{ne}
Phonon-ensemble	E_N^{de}
Magnon-phonon	E_N^{nd}

system; therefore, entanglement can exist in any combination of two modes. Interestingly, we observe promising results for macroscopic distant entanglement, i.e., the entanglement of the atomic ensemble and cavity-1 photons with phonon and magnon modes of the YIG sphere placed in cavity 2. We also illustrate entanglement transfer from the phonon-ensemble (de) and magnon-ensemble (ne) subsystems to cavity-1 photon-phonon ($a_1 d$) and cavity-1 photon-magnon ($a_1 n$) subsystems when detuning parameters and cavity-cavity coupling strength are changed. In Table I, we summarize the symbols we adopt in our simulations to represent the bipartite entanglement of different combinations of subsystems.

In Fig. 2, we present four different distant bipartite entanglements as a function of dimensionless detuning of cavity 1 (Δ_1/ω_d) and cavity 2 (Δ_2/ω_d). We consider magnon detuning $\tilde{\Delta}_n$ to be $0.9\omega_d$ (near resonant with a blue sideband), while coupling between the two cavities is $J = 0.8\omega_d$. Figures 2(a) and 2(b) illustrate ensemble-phonon (E_N^{de}) and ensemble-magnon (E_N^{ne}) entanglement for ensemble detuning Δ_e as $-\omega_d$ (resonant with a red sideband). Although the ensemble and YIG sphere are placed in separate cavities, we find strong entanglement for both E_N^{de} and E_N^{ne} . E_N^{de} attains its maximum value around $\Delta_2 \approx -1.5\omega_d$ and $\Delta_2 \approx 0$, corresponding to $\Delta_1 \approx -2\omega_d$ and $\Delta_1 \approx -0.5\omega_d$. It can be seen that E_N^{ne} manifests primarily around $\Delta_2 \approx -\omega_d$ in the

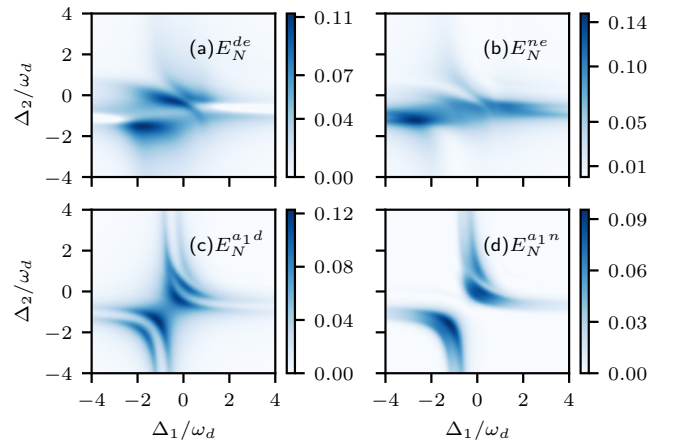


FIG. 2. Density plots of bipartite entanglements (a) E_N^{de} , (b) E_N^{ne} , (c) $E_N^{a_1 d}$, and (d) $E_N^{a_1 n}$ versus normalized cavity-1 detuning Δ_1/ω_d and cavity-2 detuning Δ_2/ω_d . In (a) and (b) $\Delta_e = -\omega_d$, whereas in (c) and (d) $\Delta_e = \omega_d$. In all cases, $\tilde{\Delta}_n = 0.9\omega_d$, and $J = 0.8\omega_d$.

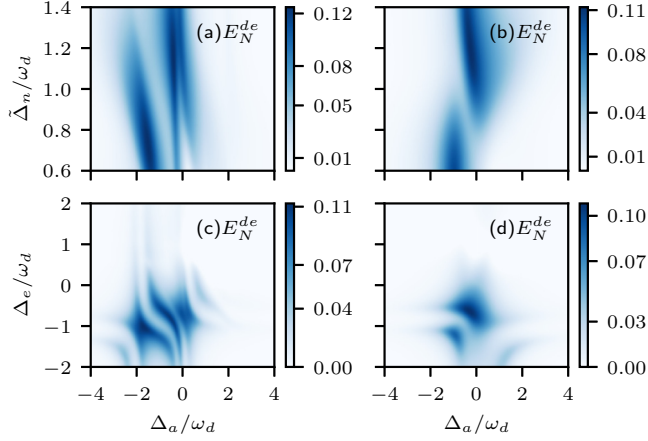


FIG. 3. Density plot of E_N^{de} versus normalized cavity detuning Δ_a/ω_d and (a) and (b) magnon detuning $\tilde{\Delta}_n/\omega_d$ at $\Delta_e = -\omega_d$ and (c) and (d) ensemble detuning Δ_e/ω_d at $\tilde{\Delta}_n = 0.9\omega_d$. In (a) and (c) $\Delta_a/\omega_d = \Delta_1/\omega_d = \Delta_2/\omega_d$. However, $\Delta_a/\omega_d = -\Delta_1/\omega_d = \Delta_2/\omega_d$ in (b) and (d). The cavity-cavity coupling strength is taken to be $J = \omega_d$.

entire range of Δ_1/ω_d . However, maximum E_N^{ne} exists around $\Delta_1 \approx -2.5\omega_d$. Similarly, we present cavity-1 photon-phonon (E_N^{a1d}) and cavity-1 photon-magnon (E_N^{a1n}) entanglement in Figs. 2(c) and 2(d) for $\Delta_e = \omega_d$. Both systems exhibit strong entanglement around $\Delta_1 \approx -\omega_d$ and $\Delta_1 \approx 0$. If we follow the $\Delta_1 = \Delta_2$ line on the plane formed by Δ_1 and Δ_2 , we observe that there are two distinct detuning regions for maximal E_N in the density plots showing E_N^{a1d} and E_N^{a1n} compared to the single joint region along the $\Delta_1 = -\Delta_2$ line.

For further analysis, we consider two cases. In the first case, cavities 1 and 2 have the same detuning frequency with respect to the frequency of the drive field, i.e., $\Delta_1 = \Delta_2 = \Delta_a$ (symmetric detuning). If the first cavity is red detuned or blue detuned, the second cavity is also red detuned or blue detuned. In the second case, cavities 1 and 2 have opposite detuning frequencies with respect to the frequency of the drive field, i.e., $\Delta_1 = -\Delta_2 = -\Delta_a$ (nonsymmetric detuning). If the first cavity is red detuned, the second is blue detuned and vice versa.

Next, we present phonon-ensemble entanglement E_N^{de} as a function of normalized cavity detuning Δ_a/ω_d against dimensionless magnon detuning $\tilde{\Delta}_n/\omega_d$ in Figs. 3(a) and 3(b) and ensemble detuning Δ_e/ω_d in Figs. 3(c) and 3(d). In the left column, we have symmetric cavity-field detuning, while in the right column, the detuning is nonsymmetric. Figures 3(a) and 3(b) show that significant entanglement is present for the complete range of effective magnon detuning. We consider $0.6 \leq \tilde{\Delta}_n/\omega_d \leq 1.4$, where we get stronger entanglement. While E_N^{de} is significant for the broad range of $\tilde{\Delta}_n$, it strongly depends on the choice of cavity-field detuning. There are two distinct regions of cavity detuning where we find maximum entanglement. One region is around cavity resonance for both the symmetric and nonsymmetric choices of detuning, while the other region depends on the choice. For the symmetric case, strong entanglement is also present around $\Delta_a \approx -1.75\omega_d$. However, for the nonsymmetric case, the second region is around $\Delta_a \approx -\omega_d$. The bottom row in

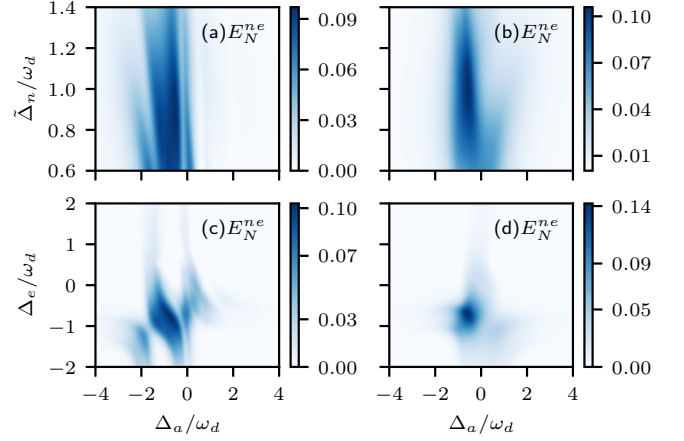


FIG. 4. Density plot of E_N^{ne} versus normalized cavity detuning Δ_a/ω_d and (a) and (b) magnon detuning $\tilde{\Delta}_n/\omega_d$ at $\Delta_e = -\omega_d$ and (c) and (d) ensemble detuning Δ_e/ω_d at $\tilde{\Delta}_n = 0.9\omega_d$. In (a) and (c) $\Delta_a/\omega_d = \Delta_1/\omega_d = \Delta_2/\omega_d$. However, $\Delta_a/\omega_d = -\Delta_1/\omega_d = \Delta_2/\omega_d$ in (b) and (d). The cavity-cavity coupling strength is taken to be $J = 0.8\omega_d$.

Fig. 3 shows that E_N^{de} is maximum around $\Delta_e \approx -\omega_d$, while the choices of cavity detuning are approximately the same as discussed above for the previous case.

Figure 4 shows magnon-ensemble entanglement E_N^{ne} as a function of normalized cavity detuning against dimensionless magnon detuning (top row) and ensemble detuning (bottom row). E_N^{ne} is optimal around $\Delta_a \approx -0.5\omega_d$. Figures 4(a) and 4(b) show that E_N^{ne} is significant for the whole range of $\tilde{\Delta}_n$, while it is maximum around $\Delta_e \approx -\omega_d$, as shown in Figs. 4(c) and 4(d). In both cases, we note that entanglement exists for a wider parameter space in symmetric detuning compared to the nonsymmetric-detuning choice. Similar to E_N^{de} , E_N^{ne} is also significant around $\Delta_e \approx -\omega_d$ and $\tilde{\Delta}_n \approx 0.9\omega_d$. As a result, we conclude that the bipartite entanglement of modes involving the atomic ensemble and YIG sphere is most remarkable when the magnon is near resonant with the

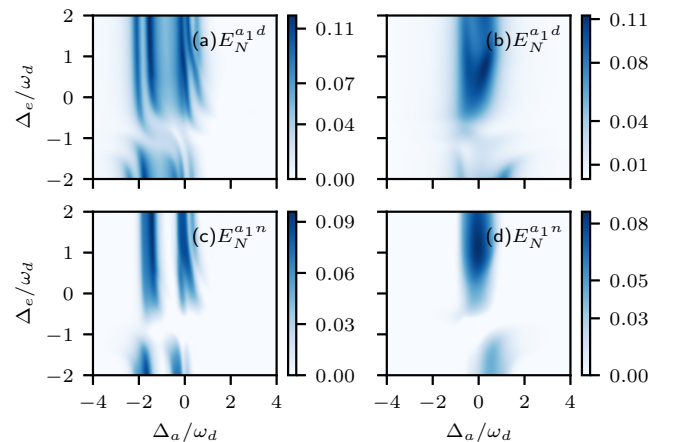


FIG. 5. Density plot of E_N^{a1d} and E_N^{a1n} versus normalized cavity detuning Δ_a/ω_d and ensemble detuning Δ_e/ω_d at $J = 0.8\omega_d$ and $\tilde{\Delta}_n = 0.9\omega_d$. In (a) and (c) $\Delta_a/\omega_d = \Delta_1/\omega_d = \Delta_2/\omega_d$. However, $\Delta_a/\omega_d = -\Delta_1/\omega_d = \Delta_2/\omega_d$ in (b) and (d).

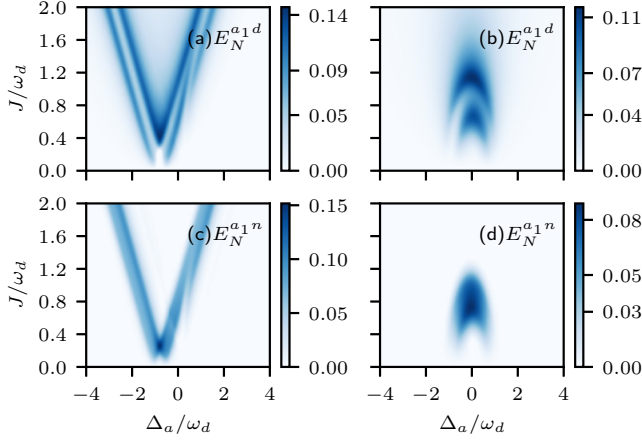


FIG. 6. Density plot of E_N^{a1d} and E_N^{a1n} versus normalized cavity detuning Δ_a/ω_d and coupling strength J/ω_d at $\tilde{\Delta}_n = 0.9\omega_d$ and $\Delta_e = \omega_d$. In (a) and (c) $\Delta_a/\omega_d = \Delta_1/\omega_d = \Delta_2/\omega_d$. However, $\Delta_a/\omega_d = -\Delta_1/\omega_d = \Delta_2/\omega_d$ in (b) and (d).

anti-Stokes band, while the ensemble is resonant with the Stokes band.

Figure 5 shows cavity-1 photon-phonon entanglement E_N^{a1d} and cavity-1 photon-magnon entanglement E_N^{a1n} as a function of normalized cavity detuning and ensemble detuning. The left column shows symmetric detuning, whereas the right column shows nonsymmetric detuning. For the symmetric case, we have significant E_N^{a1d} and E_N^{a1n} around $\Delta_a \approx -2\omega_d$ and $\Delta_a \approx 0$ for a wide range of Δ_e [see Figs. 5(a) and 5(c)]. For the second case [see Figs. 5(b) and 5(d)], E_N^{a1d} and E_N^{a1n} are significant around the resonance frequency of both cavities. In contrast to E_N^{de} and E_N^{ne} , both E_N^{a1d} and E_N^{a1n} are prominent when the atomic ensemble is resonant with the anti-Stokes sideband, i.e., at $\Delta_e \approx \omega_d$, and almost negligible at $\Delta_e = -\omega_d$ (the Stokes sideband), as depicted in Fig. 5.

We illustrate the dependence of cavity-1 photon-phonon entanglement E_N^{a1d} and cavity-1 photon-magnon entanglement E_N^{a1n} on cavity-cavity coupling strength J and cavity detuning Δ_a in Fig. 6, where we choose $\tilde{\Delta}_n = 0.9\omega_d$ and $\Delta_e = \omega_d$. As expected, the bipartite entanglement of these subsystems is nonexistent in the absence of cavity-cavity coupling. For the symmetric cavity detuning [see Figs. 6(a) and 6(c)], entanglement first increases with increasing J around $\Delta_a \approx -0.5\omega_d$; however, beyond a certain value, any further increase in J shifts the detuning region for optimal entanglement to the right and left of $\Delta_a \approx -0.5\omega_d$. However, for the nonsymmetric detuning [see Figs. 6(b) and 6(d)] the trend is quite different. Here, E_N^{a1d} and E_N^{a1n} increase with increasing coupling strength J until a particular value. We note that the dependence on J varies when different values of Δ_e and $\tilde{\Delta}_n$ are considered. For the given parameters, E_N^{a1d} first increases as a function of J , reaching a local maximum at $J \approx 0.65\omega_d$ at resonance, followed by a downtrend from $J \approx 0.65\omega_d$ to $J \approx 0.9\omega_d$, after which it increases again up to $J \approx 1.12\omega_d$ and decreases afterwards. On the other hand, E_N^{a1n} attains its maximum value from $J \approx 0.5\omega_d$ to $J \approx 0.75\omega_d$; then it decreases gradually to $J \approx 1.25\omega_d$ and dies out thereafter. It is important to note that there is a downtrend in E_N^{a1d} around $J = 0.9\omega_d$, which gives a significant value for E_N^{a1n} . The reason lies

TABLE II. Optimized parameters for E_N^{a1n} , E_N^{a1d} , E_N^{ne} , and E_N^{de} used in Fig. 8.

Subsystem	Δ_1	Δ_2	$\tilde{\Delta}_n$	Δ_e	J
E_N^{a1n}	$-1.41\omega_d$	$-0.68\omega_d$	$0.65\omega_d$	$-1.63\omega_d$	$0.35\omega_d$
E_N^{a1d}	$-0.04\omega_d$	$0.85\omega_d$	$0.77\omega_d$	$0.99\omega_d$	$1.28\omega_d$
E_N^{ne}	$0.76\omega_d$	$-0.52\omega_d$	$0.77\omega_d$	$-0.63\omega_d$	$0.8\omega_d$
E_N^{de}	$0.28\omega_d$	$-0.84\omega_d$	$0.6\omega_d$	$-1.07\omega_d$	$1.06\omega_d$

in the entanglement transfer between the different subsystems, which is further elaborated in the following analysis.

To study entanglement transfer, we set $-\Delta_1 = \Delta_2 = \Delta_a$ in our simulations. The role of J in the degree and dynamics of entanglement transfer between different subsystems is further elaborated in Fig. 7. At smaller values of cavity-cavity coupling J , the cavity-2 modes are significantly entangled (see E_N^{nd} , E_N^{a2d} , and E_N^{a2n}) around $\Delta_2 = -\omega_d$. When the coupling is increased, the cavity-1 photon and cavity-2 photon interact with each other, resulting in a redistribution of cavity photon excitations which translates to the other excitation modes. For instance, at $\Delta_2 = -\omega_d$, E_N^{nd} and E_N^{a2d} decrease with increasing cavity-cavity coupling, while most of the other bipartite entanglements increase (see the Appendix for details). Not only does this transfer decrease with increasing J , but there is also a corresponding decrease in the strength of E_N^{a2d} and E_N^{a2n} . This decrease accounts for the corresponding increase in E_N^{de} , E_N^{ne} , and E_N^{a1d} . Another interesting feature is that at smaller J , maximum entanglement of E_N^{a2d} , E_N^{a2n} , E_N^{de} , and E_N^{ne} subsystems lies around the detuning region when cavity 1 is resonant with the anti-Stokes sideband while cavity 2 is resonant with the Stokes sideband. However, the peaks of E_N curves representing their entanglement gradually shift from $\Delta_a \approx -\omega_d$ toward $\Delta_a \approx 0$ as we move from $J = 0.4\omega_d$ to $J = 1.4\omega_d$ and the region for the existence of entanglement also broadens. Since we consider $\Delta_e = -\omega_d$ in Fig. 7, E_N^{a1d} and E_N^{a1n} entanglement is quite weak in this parametric domain. Nonetheless, it is apparent that E_N^{a1d} and E_N^{a1n} entanglement also increases with increasing J , reaching a peak value followed by a decreasing trend (see the Appendix for details).

Next, we present the results of our numerical simulations, demonstrating the critical temperature T_c for E_N^{de} , E_N^{ne} , E_N^{a1d} , and E_N^{a1n} in Fig. 8. Entangled magnon-ensemble and phonon-ensemble subsystems exhibit the most robust entanglement against temperature, which can last up to 200 mK. On the other hand, cavity-1 photon-magnon entanglement can survive temperatures up to 180 mK. However, the cavity-1 photon-phonon subsystem can sustain entanglement to a temperature as high as 170 mK. Each curve in Fig. 8 is plotted for an optimized set of parameter values given in Table II.

It is important to determine how the strength of cavity-cavity coupling J impacts the robustness of distant entanglement against temperature. In Fig. 9, we present density plots of E_N^{de} , E_N^{ne} , E_N^{a1d} , and E_N^{a1n} as a function of temperature T and cavity-cavity coupling J . We infer from Fig. 9 that T_c for the existence of entanglement varies with J . The maximum value of J corresponding to maximal E_N^{de} [see Fig. 9(a)], E_N^{ne} [see Fig. 9(b)], E_N^{a1d} [see Fig. 9(c)], and E_N^{a1n} [see Fig. 9(d)] is

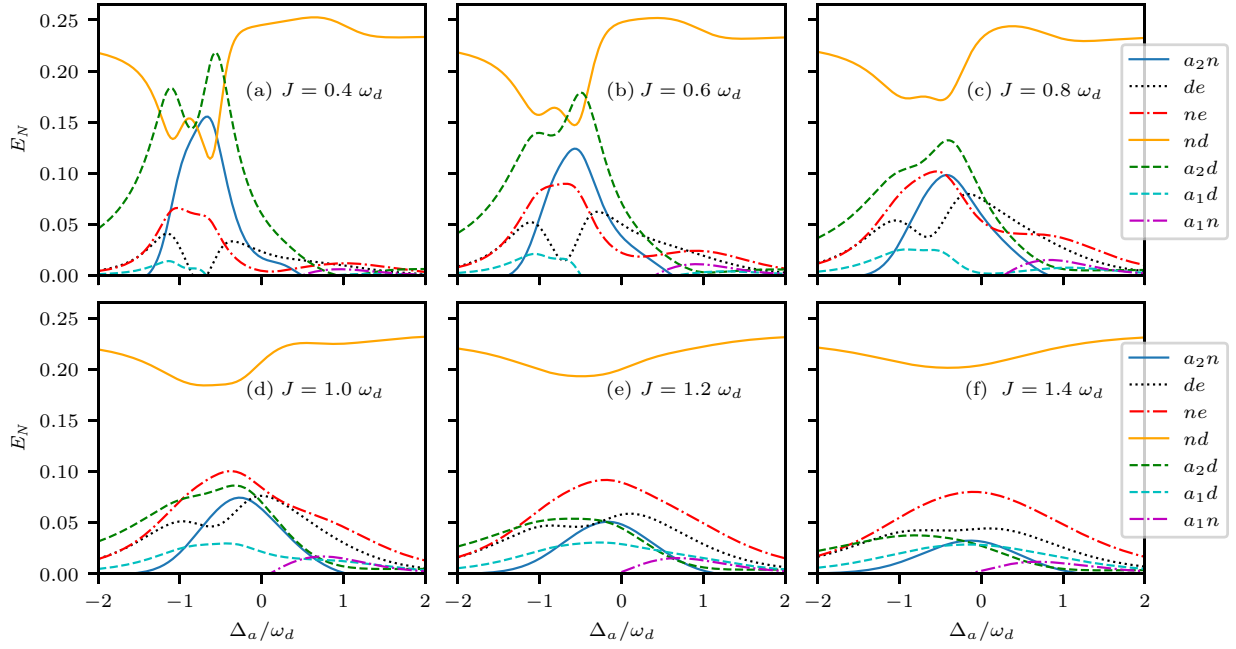


FIG. 7. Line plots illustrating the effect of the cavity-cavity coupling rate J against cavity detuning $\Delta_a/\omega_d = -\Delta_1/\omega_d = \Delta_2/\omega_d$ on bipartite entanglement of the cavity-2 photon-magnon (a_2n), phonon-ensemble (de), magnon-ensemble (ne), magnon-phonon (nd), cavity-2 photon-phonon (a_2d), cavity-1 photon-phonon (a_1d), and cavity-1 photon-magnon (a_1n) modes varied in regular intervals from $J = 0.4\omega_d$ to $J = 1.4\omega_d$ in (a)–(f) at $\tilde{\Delta}_n = 0.9\omega_d$ and $\Delta_e = -\omega_d$.

$1.06\omega_d$, $0.8\omega_d$, $1.28\omega_d$, and $0.35\omega_d$, respectively. We observe that T_c is maximum, corresponding to J for which the degree of entanglement is maximal at $T = 0$. Hence, we can say T_c can be increased through a proper choice of parameters. Apart from the bipartite entanglement of different subsystems in coupled magnomechanical system, we show that genuine tripartite entanglement can also be realized for indirectly coupled subsystems. The same magnomechanical system without cavity 1 was recently considered by Li *et al.* [25], and they showed that the tripartite magnon-phonon-photon

entanglement exists when $\tilde{\Delta}_n \simeq 0.9\omega_d$ (anti-Stokes sideband) and $\Delta_a \simeq -\omega_d$ (Stokes sideband). In the coupled magnomechanical system, we consider magnon-phonon-ensemble (nde) and cavity-1 photon-phonon-magnon (a_1dn) tripartite subsystems and plot the minimum of the residual contangle in Fig. 10 as a function of normalized detuning Δ_a/ω_d . Both these entanglements nde and a_1dn exist for a significant range of cavity-field detuning with maximum values near the resonant frequency. Interestingly, cavity-1 photon-phonon-magnon entanglement has approximately the same degree of entanglement as found in the single-cavity case [25].

In the coupled cavity scheme, future investigations may incorporate the inclusion of cross-Kerr nonlinearity [63,64],

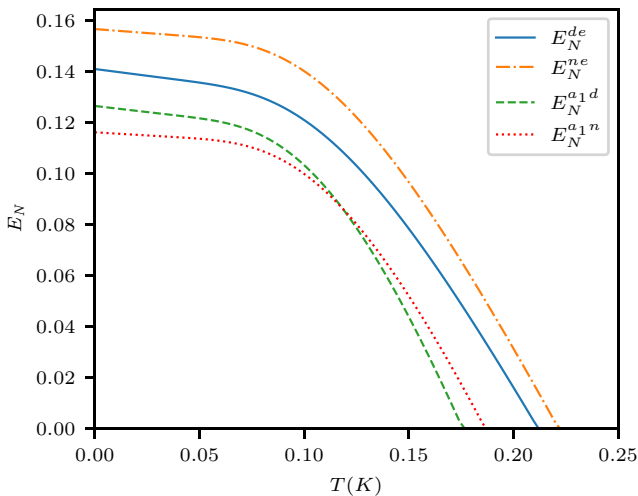


FIG. 8. Line plots for E_N^{de} , E_N^{ne} , $E_N^{a_1d}$, and $E_N^{a_1n}$ as a function of temperature considered at the optimized values of cavity detunings Δ_1 and Δ_2 , effective magnon detuning $\tilde{\Delta}_n$, ensemble detuning Δ_e , and cavity-cavity coupling rate J shown in Table II.

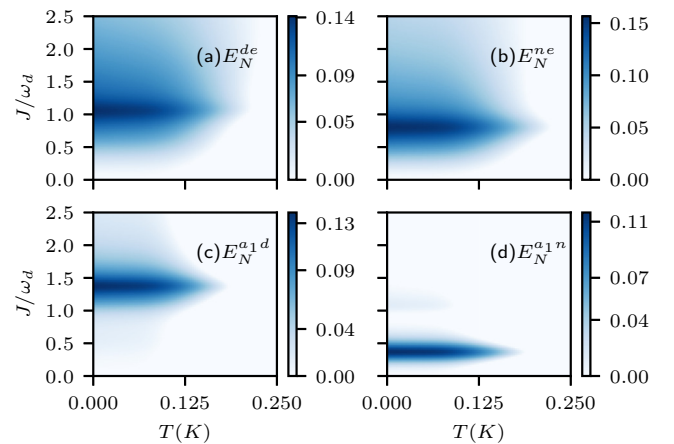


FIG. 9. Density plots of (a) E_N^{de} , (b) E_N^{ne} (c) $E_N^{a_1d}$, and (d) $E_N^{a_1n}$ as a function of temperature T and normalized coupling rate J/ω_d . Other parameters are optimized as shown in Table II.

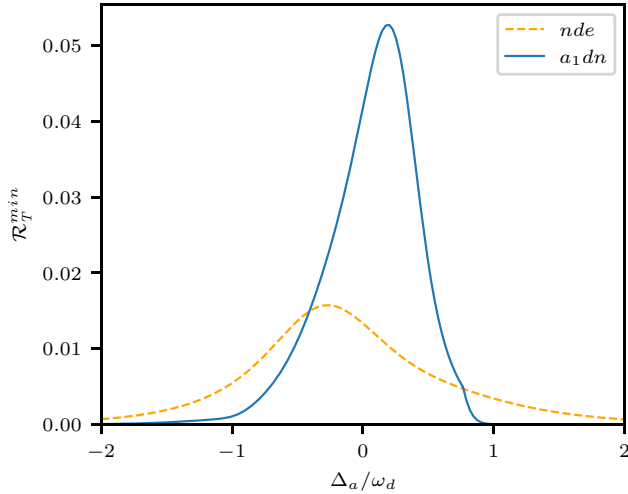


FIG. 10. Tripartite entanglement of the cavity-1 photon-magnon-phonon (a_1dn) and ensemble-magnon-phonon (nde) modes as a function of $\Delta_a/\omega_d = -\Delta_1/\omega_d = \Delta_2/\omega_d$ at $\Delta_e = 2\omega_d$ and $\tilde{\Delta}_n = 0.25\omega_d$ for a_1dn and $\Delta_e = -0.5\omega_d$ and $\tilde{\Delta}_n = 0.65\omega_d$ for nde tripartite subsystems. The cavity-cavity coupling strength is $J = \omega_d$.

the exploration of entanglement dynamics in the ultrastrong-coupling regime [65], a study of Einstein-Podolsky-Rosen steering [66], and the introduction of an optical parametric amplifier to widen the parametric regime for entanglement [67]. Furthermore, the noise-induced decoherence can be curtailed by purification and entanglement concentration in a practical long-distance quantum communication network [68,69].

IV. CONCLUSION

We proposed a scheme to realize distant entanglement between various excitation modes of the YIG sphere, atomic ensemble, and microwave modes of two coupled cavities housing an atomic ensemble and a YIG sphere. We showed that ensemble-phonon and ensemble-magnon distant bipartite entanglements not only exist but can persist up to a temperature of 200 mK with the proper choice of experimentally feasible parameters. Similarly, the entanglement of magnon and phonon modes with cavity-1 photons is also robust up to a temperature of about 170 mK. Most importantly, we demonstrated that two types of tripartite entanglement between different distant modes are possible in the proposed system. They include magnon-phonon-ensemble and cavity-1 photon-phonon-magnon entanglements. Interestingly, the strength of cavity-1 photon-phonon-magnon tripartite entanglement is comparable to the originally proposed photon-phonon-magnon tripartite entanglement of the same cavity modes. Hence, we conclude that both the bipartite and tripartite entanglements between indirectly coupled systems are substantial in our proposed setup. Moreover, cavity-cavity coupling strength plays a key role in the degree of entanglement as well as the range of parameters in which it subsists. We believe that the parametric regimes identified in our proposed system may prove useful for the experimental realization of distant entanglement, which is significant for processing continuous-variable quantum information in quantum memory protocols.

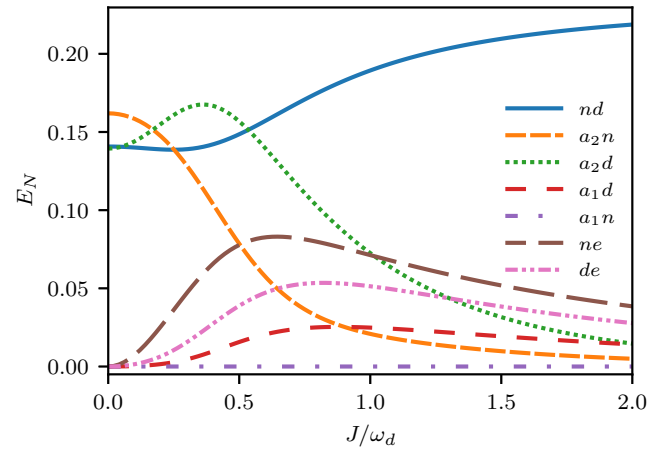


FIG. 11. Line plot of E_N against the cavity-cavity coupling rate J . The rest of the conditions and parameters are the same as in Fig. 7 with $\Delta_a = -\omega_d$.

APPENDIX: ENTANGLEMENT TRANSFER

Here, we further discuss the entanglement transfer phenomenon studied in Fig. 7. In Fig. 11, we plot bipartite entanglements as a function of cavity-cavity coupling J at $\Delta_a = -\omega_d$. It can be seen that when $J = 0$, we have entanglement between only three modes of cavity 2 since cavity 1 is decoupled. When cavity-cavity coupling is turned on, the cavity fields interact with each other. As a result, the populations of various modes change, leading to the transfer of entanglement between different modes. Figure 11 shows that initially, E_N^{nd} and $E_N^{a_2n}$ decrease with an increase in $E_N^{a_2d}$, $E_N^{a_1d}$, $E_N^{a_1n}$, and E_N^{de} . A further increase in J leads to a decreasing trend in $E_N^{a_2d}$. On the other hand, cavity-1 photon-magnon ($E_N^{a_1n}$) entanglement increases as a function of J around $\Delta_a \approx \omega_d$, reaching a maximum followed by a decaying trend, as shown in Fig. 12(b). Similarly, Fig. 12(a) illustrates a similar trend for the cavity-1 photon-phonon entanglement, reaching a peak value near resonance, followed by the decaying trend. Besides the increase in entanglement amplitude, the domain of entanglement in the detuning space also increases.

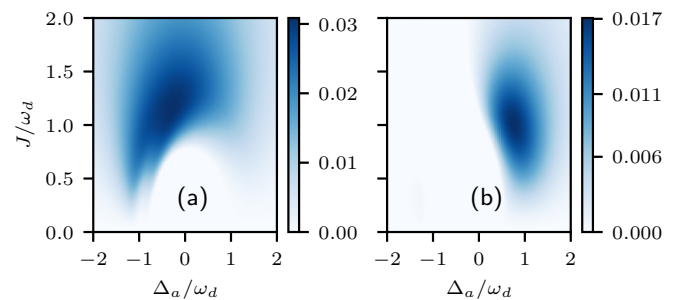


FIG. 12. Density plots illustrating the effect of the cavity-cavity coupling rate J and cavity detuning Δ_a on bipartite entanglement of (a) the cavity-1 photon-phonon (a_1d) and (b) cavity-1 photon-magnon (a_1n) modes. The rest of the conditions and parameters are the same as in Fig. 7.

- [1] R. Horodecki, P. Horodecki, M. Horodecki, and K. Horodecki, Quantum entanglement, *Rev. Mod. Phys.* **81**, 865 (2009).
- [2] F. Fröwis, P. Sekatski, W. Dür, N. Gisin, and N. Sangouard, Macroscopic quantum states: Measures, fragility, and implementations, *Rev. Mod. Phys.* **90**, 025004 (2018).
- [3] H. J. Kimble, The quantum internet, *Nature (London)* **453**, 1023 (2008).
- [4] C. Simon, Towards a global quantum network, *Nat. Photon.* **11**, 678 (2017).
- [5] C. B. Møller, R. A. Thomas, G. Vasilakis, E. Zeuthen, Y. Tsaturyan, M. Balabas, K. Jensen, A. Schliesser, K. Hammerer, and E. S. Polzik, Quantum back-action-evading measurement of motion in a negative mass reference frame, *Nature (London)* **547**, 191 (2017).
- [6] M. Lukin, M. Fleischhauer, and A. Imamoglu, Quantum information processing based on cavity QED with mesoscopic systems, in *Directions in Quantum Optics*, edited by H. J. Carmichael, R. J. Glauber, and M. O. Scully (Springer, Berlin, 2001).
- [7] M. Aspelmeyer, T. J. Kippenberg, and F. Marquardt, Cavity optomechanics, *Rev. Mod. Phys.* **86**, 1391 (2014).
- [8] I. Favero and F. Marquardt, Focus on optomechanics, *New J. Phys.* **16**, 085006 (2014).
- [9] I. Favero and K. Karrai, Optomechanics of deformable optical cavities, *Nat. Photon.* **3**, 201 (2009).
- [10] P. Meystre, A short walk through quantum optomechanics, *Ann. Phys. (Berlin, Ger.)* **525**, 215 (2013).
- [11] Y.-D. Wang and A. A. Clerk, Using dark modes for high-fidelity optomechanical quantum state transfer, *New J. Phys.* **14**, 105010 (2012).
- [12] A. Mari and J. Eisert, Opto- and electro-mechanical entanglement improved by modulation, *New J. Phys.* **14**, 075014 (2012).
- [13] N. Sangouard, C. Simon, H. de Riedmatten, and N. Gisin, Quantum repeaters based on atomic ensembles and linear optics, *Rev. Mod. Phys.* **83**, 33 (2011).
- [14] Y. Tabuchi, S. Ishino, T. Ishikawa, R. Yamazaki, K. Usami, and Y. Nakamura, Hybridizing ferromagnetic magnons and microwave photons in the quantum limit, *Phys. Rev. Lett.* **113**, 083603 (2014).
- [15] H. Huebl, C. W. Zollitsch, J. Lotze, F. Hocke, M. Greifenstein, A. Marx, R. Gross, and S. T. B. Goennenwein, High cooperativity in coupled microwave resonator ferrimagnetic insulator hybrids, *Phys. Rev. Lett.* **111**, 127003 (2013).
- [16] L. Wang, Z. Lu, X. Zhao, W. Zhang, Y. Chen, Y. Tian, S. Yan, L. Bai, and M. Harder, Magnetization coupling in a YIG/GGG structure, *Phys. Rev. B* **102**, 144428 (2020).
- [17] M. Goryachev, W. G. Farr, D. L. Creedon, Y. Fan, M. Kostylev, and M. E. Tobar, High-cooperativity cavity QED with magnons at microwave frequencies, *Phys. Rev. Appl.* **2**, 054002 (2014).
- [18] L. Bai, M. Harder, Y. P. Chen, X. Fan, J. Q. Xiao, and C.-M. Hu, Spin pumping in electro-dynamically coupled magnon-photon systems, *Phys. Rev. Lett.* **114**, 227201 (2015).
- [19] R. Hisatomi, A. Osada, Y. Tabuchi, T. Ishikawa, A. Noguchi, R. Yamazaki, K. Usami, and Y. Nakamura, Bidirectional conversion between microwave and light via ferromagnetic magnons, *Phys. Rev. B* **93**, 174427 (2016).
- [20] A. Osada, R. Hisatomi, A. Noguchi, Y. Tabuchi, R. Yamazaki, K. Usami, M. Sadgrove, R. Yalla, M. Nomura, and Y. Nakamura, Cavity optomagnonics with spin-orbit coupled photons, *Phys. Rev. Lett.* **116**, 223601 (2016).
- [21] J. A. Haigh, A. Nunnenkamp, A. J. Ramsay, and A. J. Ferguson, Triple-resonant Brillouin light scattering in magneto-optical cavities, *Phys. Rev. Lett.* **117**, 133602 (2016).
- [22] D. Lachance-Quirion, Y. Tabuchi, S. Ishino, A. Noguchi, T. Ishikawa, R. Yamazaki, and Y. Nakamura, Resolving quanta of collective spin excitations in a millimeter-sized ferromagnet, *Sci. Adv.* **3**, e1603150 (2017).
- [23] Y.-P. Wang, G.-Q. Zhang, D. Zhang, T.-F. Li, C.-M. Hu, and J. Q. You, Bistability of cavity magnon polaritons, *Phys. Rev. Lett.* **120**, 057202 (2018).
- [24] Y. Tabuchi, S. Ishino, A. Noguchi, T. Ishikawa, R. Yamazaki, K. Usami, and Y. Nakamura, Coherent coupling between a ferromagnetic magnon and a superconducting qubit, *Science* **349**, 405 (2015).
- [25] J. Li, S.-Y. Zhu, and G. S. Agarwal, Magnon-photon-phonon entanglement in cavity magnomechanics, *Phys. Rev. Lett.* **121**, 203601 (2018).
- [26] J. Li and S.-Y. Zhu, Entangling two magnon modes via magnetostrictive interaction, *New J. Phys.* **21**, 085001 (2019).
- [27] W.-J. Wu, Y.-P. Wang, J.-Z. Wu, J. Li, and J. Q. You, Remote magnon entanglement between two massive ferrimagnetic spheres via cavity optomagnonics, *Phys. Rev. A* **104**, 023711 (2021).
- [28] C.-X. Ning and M. Yin, Entangling magnon and superconducting qubit by using a two-mode squeezed-vacuum microwave field, *J. Opt. Soc. Am. B* **38**, 3020 (2021).
- [29] N. Wang, Z.-B. Yang, S.-Y. Li, Y.-L. Tong, and A.-D. Zhu, Non-reciprocal transmission and asymmetric entanglement induced by magnetostriction in a cavity magnomechanical system, *Eur. Phys. J. Plus* **137**, 422 (2022).
- [30] Y.-L. Ren, J.-K. Xie, X.-K. Li, S.-L. Ma, and F.-L. Li, Long-range generation of a magnon-magnon entangled state, *Phys. Rev. B* **105**, 094422 (2022).
- [31] Y. Chen, Macroscopic quantum mechanics: Theory and experimental concepts of optomechanics, *J. Phys. B* **46**, 104001 (2013).
- [32] C. Joshi, J. Larson, M. Jonson, E. Andersson, and P. Öhberg, Entanglement of distant optomechanical systems, *Phys. Rev. A* **85**, 033805 (2012).
- [33] U. Akram, W. Munro, K. Nemoto, and G. J. Milburn, Photon-phonon entanglement in coupled optomechanical arrays, *Phys. Rev. A* **86**, 042306 (2012).
- [34] W. Ge, M. Al-Amri, H. Nha, and M. S. Zubairy, Entanglement of movable mirrors in a correlated-emission laser, *Phys. Rev. A* **88**, 022338 (2013).
- [35] J.-Q. Liao, Q.-Q. Wu, and F. Nori, Entangling two macroscopic mechanical mirrors in a two-cavity optomechanical system, *Phys. Rev. A* **89**, 014302 (2014).
- [36] A. A. Rehaily and S. Bougouffa, Entanglement generation between two mechanical resonators in two optomechanical cavities, *Int. J. Theor. Phys.* **56**, 1399 (2017).
- [37] C.-H. Bai, D.-Y. Wang, H.-F. Wang, A.-D. Zhu, and S. Zhang, Robust entanglement between a movable mirror and atomic ensemble and entanglement transfer in coupled optomechanical system, *Sci. Rep.* **6**, 33404 (2016).
- [38] G. Li, W. Nie, Y. Wu, Q. Liao, A. Chen, and Y. Lan, Manipulating the steady-state entanglement via three-level atoms in a hybrid levitated optomechanical system, *Phys. Rev. A* **102**, 063501 (2020).

- [39] H. Ian, Z. R. Gong, Y.-X. Liu, C. P. Sun, and F. Nori, Cavity optomechanical coupling assisted by an atomic gas, *Phys. Rev. A* **78**, 013824 (2008).
- [40] L. Zhou, Y. Han, J. Jing, and W. Zhang, Entanglement of nanomechanical oscillators and two-mode fields induced by atomic coherence, *Phys. Rev. A* **83**, 052117 (2011).
- [41] Z.-Y. Fan, H. Qian, X. Zuo, and J. Li, Entangling ferrimagnetic magnons with an atomic ensemble via optomagnomechanics, *Phys. Rev. A* **108**, 023501 (2023).
- [42] Y. Wu, J.-H. Liu, Y.-F. Yu, Z.-M. Zhang, and J.-D. Wang, Entangling a magnon and an atomic ensemble mediated by an optical cavity, *Phys. Rev. Appl.* **20**, 034043 (2023).
- [43] C. Genes, D. Vitali, and P. Tombesi, Emergence of atom-light-mirror entanglement inside an optical cavity, *Phys. Rev. A* **77**, 050307(R) (2008).
- [44] J. Hald, J. L. Sørensen, C. Schori, and E. S. Polzik, Spin squeezed atoms: A macroscopic entangled ensemble created by light, *Phys. Rev. Lett.* **83**, 1319 (1999).
- [45] X. Zhang, C.-L. Zou, L. Jiang, and H. X. Tang, Cavity magnomechanics, *Sci. Adv.* **2**, e1501286 (2016).
- [46] S.-B. Zheng, Generation of atomic and field squeezing by adiabatic passage and symmetry breaking, *Phys. Rev. A* **86**, 013828 (2012).
- [47] T. Holstein and H. Primakoff, Field dependence of the intrinsic domain magnetization of a ferromagnet, *Phys. Rev.* **58**, 1098 (1940).
- [48] K. Hammerer, A. S. Sørensen, and E. S. Polzik, Quantum interface between light and atomic ensembles, *Rev. Mod. Phys.* **82**, 1041 (2010).
- [49] X. Zhang, C.-L. Zou, L. Jiang, and H. X. Tang, Strongly coupled magnons and cavity microwave photons, *Phys. Rev. Lett.* **113**, 156401 (2014).
- [50] A. A. Clerk, M. H. Devoret, S. M. Girvin, F. Marquardt, and R. J. Schoelkopf, Introduction to quantum noise, measurement, and amplification, *Rev. Mod. Phys.* **82**, 1155 (2010).
- [51] C. Genes, A. Mari, P. Tombesi, and D. Vitali, Robust entanglement of a micromechanical resonator with output optical fields, *Phys. Rev. A* **78**, 032316 (2008).
- [52] A. Nunnenkamp, K. Børkje, and S. M. Girvin, Single-photon optomechanics, *Phys. Rev. Lett.* **107**, 063602 (2011).
- [53] M. Ludwig, B. Kubala, and F. Marquardt, The optomechanical instability in the quantum regime, *New J. Phys.* **10**, 095013 (2008).
- [54] S. Qvarfort, M. R. Vanner, P. F. Barker, and D. E. Bruschi, Master-equation treatment of nonlinear optomechanical systems with optical loss, *Phys. Rev. A* **104**, 013501 (2021).
- [55] M. Ludwig, K. Hammerer, and F. Marquardt, Entanglement of mechanical oscillators coupled to a nonequilibrium environment, *Phys. Rev. A* **82**, 012333 (2010).
- [56] E. X. DeJesus and C. Kaufman, Routh-Hurwitz criterion in the examination of eigenvalues of a system of nonlinear ordinary differential equations, *Phys. Rev. A* **35**, 5288 (1987).
- [57] P. C. Parks and V. Hahn, *Stability Theory* (Prentice Hall, New York, 1993).
- [58] M. B. Plenio, Logarithmic negativity: A full entanglement monotone that is not convex, *Phys. Rev. Lett.* **95**, 090503 (2005).
- [59] G. Vidal and R. F. Werner, Computable measure of entanglement, *Phys. Rev. A* **65**, 032314 (2002).
- [60] R. Simon, Peres-Horodecki separability criterion for continuous variable systems, *Phys. Rev. Lett.* **84**, 2726 (2000).
- [61] G. Adesso and F. Illuminati, Continuous variable tangle, monogamy inequality, and entanglement sharing in Gaussian states of continuous variable systems, *New J. Phys.* **8**, 15 (2006).
- [62] V. Coffman, J. Kundu, and W. K. Wootters, Distributed entanglement, *Phys. Rev. A* **61**, 052306 (2000).
- [63] R.-C. Shen, J. Li, Z.-Y. Fan, Y.-P. Wang, and J. Q. You, Mechanical bistability in Kerr-modified cavity magnomechanics, *Phys. Rev. Lett.* **129**, 123601 (2022).
- [64] Y.-B. Sheng, F.-G. Deng, and H.-Y. Zhou, Efficient polarization-entanglement purification based on parametric down-conversion sources with cross-Kerr nonlinearity, *Phys. Rev. A* **77**, 042308 (2008).
- [65] Y. S. Teo and J. Gong, Double Rabi model in the ultra-strong coupling regime: Entanglement and chaos beyond the rotating wave approximation, *J. Phys. B* **46**, 235504 (2013).
- [66] H. Tan and J. Li, Einstein-Podolsky-Rosen entanglement and asymmetric steering between distant macroscopic mechanical and magnonic systems, *Phys. Rev. Res.* **3**, 013192 (2021).
- [67] B. Hussain, S. Qamar, and M. Irfan, Entanglement enhancement in cavity magnomechanics by an optical parametric amplifier, *Phys. Rev. A* **105**, 063704 (2022).
- [68] C. H. Bennett, G. Brassard, S. Popescu, B. Schumacher, J. A. Smolin, and W. K. Wootters, Purification of noisy entanglement and faithful teleportation via noisy channels, *Phys. Rev. Lett.* **76**, 722 (1996).
- [69] T. Yamamoto, M. Koashi, and N. Imoto, Concentration and purification scheme for two partially entangled photon pairs, *Phys. Rev. A* **64**, 012304 (2001).